

# Prompt and Conventional High-Energy Muon Spectra from a full Monte Carlo Simulation via **CORSIKA7**

Ludwig Neste <sup>1,2\*</sup>, Pascal Gutjahr <sup>1,5\*</sup>, Mirco Hünnefeld <sup>1,5,6</sup>,  
Jean-Marco Alameddine <sup>1,5</sup>, Wolfgang Rhode <sup>1,3,5</sup>, Julia Becker Tjus <sup>3,4,5,7</sup>,  
Felix Riehn <sup>1</sup>, Kevin Kröninger <sup>1,3</sup>, Johannes Albrecht <sup>1,3,5</sup>

<sup>1</sup>\*Department of Physics, TU Dortmund University, Dortmund, 44227, Germany.

<sup>2</sup>Oskar Klein Centre and Department of Physics, Stockholm University, Stockholm, 10691, Sweden.

<sup>3</sup>Ruhr Astroparticle and Plasma Physics Center (RAPP Center), Germany.

<sup>4</sup>Theoretical Physics IV: Plasma Astroparticle Physics, Ruhr University Bochum, Bochum, 44780, Germany.

<sup>5</sup>Lamarr Institute for Machine Learning and Artificial Intelligence, Germany.

<sup>6</sup>Department of Astronomy, University of Wisconsin—Madison, Madison, WI 53706, USA.

<sup>7</sup>Department of Space, Earth and Environment, Chalmers University of Technology, 412 96 Gothenburg, Sweden.

\*Corresponding author(s). E-mail(s): [ludwig.neste@fysik.su.se](mailto:ludwig.neste@fysik.su.se);  
[pascal.gutjahr@tu-dortmund.de](mailto:pascal.gutjahr@tu-dortmund.de);

Contributing authors: [mirco.huennefeld@tu-dortmund.de](mailto:mirco.huennefeld@tu-dortmund.de);  
[jean-marco.alameddine@tu-dortmund.de](mailto:jean-marco.alameddine@tu-dortmund.de); [wolfgang.rhode@tu-dortmund.de](mailto:wolfgang.rhode@tu-dortmund.de);  
[julia.tjus@tu-dortmund.de](mailto:julia.tjus@tu-dortmund.de); [felix.riehn@tu-dortmund.de](mailto:felix.riehn@tu-dortmund.de);  
[kevin.kroeninger@tu-dortmund.de](mailto:kevin.kroeninger@tu-dortmund.de); [johannes.albrecht@tu-dortmund.de](mailto:johannes.albrecht@tu-dortmund.de);

## Abstract

Extensive air showers produce high-energy muons that can be utilized to probe hadronic interaction models in cosmic ray interactions. Most muons originate from pion and kaon decays, called *conventional* muons, while a smaller fraction, referred to as *prompt* muons, arises from the decay of heavier, short-lived hadrons. The EHISTORY option of the air shower simulation tool CORSIKA7 is used in this work to investigate the prompt and conventional muon flux in the energy range of 100 TeV to 100 PeV, utilizing the newly developed open-source python software PANAMA. Identifying the muon parent particles allows for scaling the contribution of prompt particles, which can be leveraged by future experimental analyses to measure the normalization of the prompt muon flux. Obtained prompt muon spectra from CORSIKA7 are compared to MCEq results. The relevance to large-volume neutrino detectors, such as IceCube and KM3NeT, and the connection to hadronic interaction models is discussed.

**Keywords:** Air Showers, Prompt Muons, CORSIKA, Hadronic Interactions

# 1 Introduction

Primary cosmic ray (CR) particles interacting with the Earth’s atmospheric nuclei initiate extensive air showers (EAS). Secondary particles, including light and heavy mesons produced in hadronic interactions, undergo further interactions and decay to generate electrons, muons, and neutrinos, called final-state leptons. Observations from both ground-based and underground experiments have shown an atmospheric muon flux that exceeds theoretical predictions towards high energies, a discrepancy referred to as the “muon puzzle” [1]. Hadronic interaction models that describe the secondary particle production in EAS are difficult to test using accelerator experiments, primarily due to the extremely high energies of CRs, reaching up to EeV [2], and the strong relativistic boost to the forward region of secondary particles. Air-shower experiments and large-volume water-Cherenkov telescopes, such as AUGER [3, 4], IceCube [5, 6], and KM3NeT [7, 8], provide an alternative approach to probe hadronic interactions and thus play a crucial role in the study of this phenomenon. By differentiating between the prompt and conventional atmospheric lepton fluxes in Monte Carlo (MC) simulations, this research aims to gain deeper insights into the muon excess. This leads to more accurate hadronic interaction models and an enhancement of our understanding of CR interactions.

This paper presents comprehensive MC simulations using the tool CORSIKA7 [9]. CORSIKA (COsmic Ray SIMulations for KAscade) is a widely used MC simulation tool designed for modeling EAS initiated by high-energy CRs. It simulates the interactions and propagation of primary cosmic particles and their secondary products, such as muons, hadrons, and electromagnetic components, through the atmosphere. It provides the secondary particles on a defined surface with resulting properties like energy, direction, and position. The tool has an option to also store the parent and grandparent particles, referred to as extended history (EHISTORY). This enables to differentiate between the prompt and conventional components, defined by their parent particles.

At first, this definition of the prompt component is discussed in Section 2, followed by an investigation of prompt muons within CORSIKA7 in Section 3. There, the results are compared

to a solution provided by the software package MCEq (Matrix Cascade Equation) [10], a numerical software package designed to solve cascade equations [11, p.107] for atmospheric particle showers. After the validation of the prompt identification, a method is outlined for determining the normalization of the prompt muon component using a detector such as IceCube or KM3NeT in Section 4. Finally, further properties of the prompt muon flux like leadingness and their relation to the primaries are studied in Section 5. Parametrizations of the muon flux originating from different groups of parent-particles are provided in Appendix B.

## 2 Definition of Prompt Leptons in Air Showers

The term prompt is defined differently across physics sub-fields. In high-energy collider physics, a prompt particle is defined as one produced directly in the primary interaction (e.g., a proton-proton collision) rather than from the decay of secondary particles [12]. In nuclear physics, a *prompt neutron* refers to a neutron directly released by nuclear fission [13].

In astroparticle physics, the categorization of particles into conventional and prompt groups depends on the lifetimes of the decaying parent particles and, thus, on the resulting energy spectra of final-state leptons [11, p. 179]. These spectra approximately follow power-law distributions of the form  $dN/dE \propto E^{-\gamma}$ , where  $\gamma$  denotes the spectral index. Prompt particles have extremely short lifetimes and most likely decay before they can interact with the atmosphere. In contrast, conventional particles have longer lifetimes, likely causing them to interact with the atmosphere before decaying. Due to relativistic time dilatation, the lifetimes increase linearly with energy, leading to an increased probability of interactions with the atmosphere. This dependence results in a softer spectrum for particles which are more likely to re-interact with the atmosphere instead of decaying, where the spectral index  $\gamma$  is reduced by 1.

By grouping parent particles according to their lifetime, the prompt component is defined as follows:

The *conventional* part of the lepton flux consists of leptons originating from  $\pi^\pm$ ,  $K^\pm$ ,  $K_L^0$ , and  $K_S^0$  decays. All other leptons are considered part of the *prompt* flux.

To distinguish the atmospheric lepton flux into prompt and conventional components in MC EAS simulations, it is essential to identify the direct parent particle type of each lepton.

This paper demonstrates how this labeling process, termed *prompt tagging*, can be applied to muons using the EAS simulation software CORSIKA7 with the EHISTORY compilation option, as described in Section 3. Although the focus is on muons in this paper, neutrinos are produced in prompt decays as well and the formalism is also applicable to neutrinos. IceCube has previously attempted to measure the normalization of the prompt component, but the simulation did not include charmed mesons, which contribute significantly to prompt muons, and the information whether a particle is prompt or conventional was not available either [14].

### 3 Tagging Prompt Particles in CORSIKA7 Simulations with PANAMA

CORSIKA7 [9] is the current standard MC software for the simulation of EAS in many astroparticle experiments. The software handles the propagation of particles through Earth’s atmosphere, including simulation of interactions and decays. The default output of CORSIKA7 includes information about the execution parameters, such as the run number and event-specific data. Each event represents one EAS and includes the direction, type, energy, and momentum of the injected primary particle, as well as a list of all observation-level particles. This list contains the Particle ID (PID), Hadron Generation Counter (HGC), observation level, momentum vector, and position and time since the first interaction for each particle reaching the observation level [15, p. 127].

With the activation of the EHISTORY option, the particle list can be extended to include two ancestors for muons and neutrinos [16]. These are termed the parent and grandparent particles<sup>1</sup> and

are marked with negative PID encoding, indicating they are not present at the observation level. Tagging prompt particles involves parsing the PID of the parent particle and tagging it as prompt if the parent is neither a pion nor a kaon (see Section 2). However, the parent particles given in CORSIKA7 are not always the direct parents of the particle at the observation level. By using the HGC, which generally increments by one with each hadronic interaction and decay, true parent particles can be distinguished from false parent particles higher up in the decay chain.

When tagging a lepton with, for example, a  $D$  meson as the parent, the tag would be prompt if the charmed meson is the true parent particle, but conventional if there were additional intermediate decays into conventional particles in between. These edge-cases as described in Ref. [16] must be taken into account in the tagging procedure. To facilitate the tagging of prompt particles in CORSIKA7 simulations, a newly developed Python package PANAMA [17] is developed and publicly available. The package primarily functions as a modern python tool for running CORSIKA7 in parallel and parsing (EHISTORY) output and was also used to generate the results presented in this paper. Additional details and examples can be found in PANAMA’s documentation<sup>2</sup>.

#### 3.1 Prompt Muon Fluxes from CORSIKA7 in Comparison to MCEq

To validate the tagging method using CORSIKA7’s EHISTORY option, as described in Section 3, a comparison with results obtained from MCEq is performed. MCEq can compute resulting muon fluxes, including dependencies on the parent particle’s PID. However, solving the 1D-cascade equations cannot provide information on the lateral distribution of particles<sup>3</sup> or shower-to-shower fluctuations. The software makes use of pre-computed tables of transition probabilities for interactions and decays, which are generated using MC event generators such as SIBYLL[20] or QGSJET[21]. While both MCEq and CORSIKA7 utilize the same underlying MC event generators to simulate particle

<sup>1</sup>Referred to as *mother* and *grandmother* particles in CORSIKA’s user guide [15]

<sup>2</sup>Software and documentation freely available at [github.com/The-Ludwig/PANAMA](https://github.com/The-Ludwig/PANAMA)

<sup>3</sup>A 2D version of MCEq is currently in development [18, 19].

interactions or decays, they differ in their methods of atmospheric propagation.

For this comparison, a dataset of over 60 million EAS is simulated using CORSIKA7. The energy spectrum from which the primary particle energy  $E_p$  is sampled follows a power-law distribution:

$$\Phi_s(E_p) = \frac{1}{N} \cdot E_p^{-\gamma_s}, \quad (1)$$

where  $N$  is a normalization constant that adjusts the probability density function (PDF) over the sampled energy range. The spectral index  $\gamma_s$  is chosen to be harder (i.e., smaller) than the expected physical spectrum to bias the simulation towards higher-energy events, thus increasing simulation efficiency.

To convert the sampled spectrum to a realistic CR spectrum,  $\Phi_p(E_p)$ , each event is weighted by the factor:

$$w = \frac{\Phi_p(E_p)}{n\Phi_s(E_p)} = \Phi_p(E_p) \cdot \frac{N}{nE_p^{-\gamma_s}}, \quad (2)$$

where  $n$  represents the total number of events generated in the energy range. Re-weighting enables testing of different models for the CR spectrum after the computationally expensive EAS simulation has been completed, with minimal additional cost. The weighting and CR fluxes are implemented in PANAMA [17]. Equation (1) can be generalized to arbitrary PDFs, but it is advantageous to select a PDF that is analytically integrable, allowing for straightforward calculation of the normalization factor  $N$  for re-weighting.

In this work, a piecewise (non-continuous) power-law distribution is used to control the prevalence of events in different energy regions. Equation (1) still applies, but must be normalized according to the number of events sampled in each energy region. To capture the transition from the conventional to the prompt muon flux, the simulated primary energy range must extend up to  $5 \cdot 10^{10}$  GeV, which approximates the energy of the most energetic CR ever measured [22].

The primary CR spectrum consists of numerous nuclei, ranging from hydrogen to iron and heavier elements [11]. In the simulation, not all nuclei are injected with a physically accurate composition. Instead, the various primaries are grouped, and for each group, the dominant nucleus

is selected to represent all showers within that group. Typically, these groups are defined such that the range of  $\log(A)$  values within each group are spaced approximately equally. This approach is motivated by the fact that the atmospheric depth at which the maximum number of secondary particles ( $X_{\max}$ ) is produced scales with  $\log(A)$  [23].

The composition is crucial for the generation of prompt leptons because the likelihood of producing high-mass hadrons in air showers depends on the interaction energy of nucleon collisions, which is determined by the per-nucleon energy of the CR, rather than its total energy.

Table 1: The statistics of the CORSIKA7 MC dataset used in this work is presented. The first column shows the nucleus energy range of the injected primary, given in the second column. The total number of generated showers  $n$  is given in the third column, which consists of the number of different primary types  $n_p$  times the two simulated zenith angles  $n_\theta$  of  $\theta = 0^\circ$  and  $\theta = 60^\circ$  times the number of events generated  $n_{\text{sim}}$ . The primaries are each sampled from a  $E^{-1}$  energy spectrum.

$E_p / \text{GeV}$	Primary	$n_p \cdot n_\theta \cdot n_{\text{sim}} = n$
$10^5 - 1 \cdot 10^9$	$^1\text{H}, ^4\text{He}, ^{12}\text{C}$	$3 \cdot 2 \cdot 10^7 = 6 \cdot 10^7$
	$^{28}\text{Si}, ^{54}\text{Fe}$	$2 \cdot 2 \cdot 10^6 = 4 \cdot 10^6$
$10^9 - 5 \cdot 10^{10}$	$^1\text{H}, ^4\text{He}, ^{12}\text{C}$	$3 \cdot 2 \cdot 10^5 = 6 \cdot 10^5$
	$^{28}\text{Si}, ^{54}\text{Fe}$	$2 \cdot 2 \cdot 10^4 = 4 \cdot 10^4$

The properties of the generated CORSIKA7 dataset are listed in Table 1 and the full steering card can be found in Appendix A. CORSIKA7 version 7.7420 is used and compiled with the CHARM, CURVED, DYNSTACK and EHISTORY options. The configured high-energy hadron model is SIBYLL2.3d [24] and the low-energy one is URQMD [25]. The prompt component of the muon flux becomes dominant above around 1 PeV. Hence, the settings are chosen such that all the muons above  $10^5$  GeV are generated. The simulated primary energy range starts at  $10^5$  GeV, and the hadron and muon cutoff is set to  $10^5$  GeV as well. This approach enables the generation of large statistics, with over 60 million showers (see

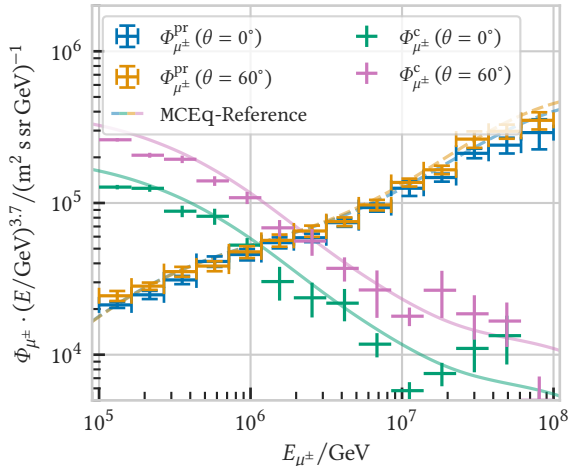


**Fig. 1:** The high energy muon spectrum produced by CORSIKA7 (crosses), divided into the prompt (orange and blue) and conventional (green and pink) component, is shown at two different zenith angles  $\theta = 0^\circ$  (vertical) and  $\theta = 60^\circ$ . The MCEq-prediction, shown in solid lines, matches the weighted CORSIKA7 histograms. Gaisser H3a (“mixed” population from Table 1 of Ref. [27]) is chosen as the primary model.

Table 1), as many low-energy muons and hadrons are excluded from the simulation. Since this work focuses on the hadronic part of EAS, the electromagnetic component (electrons and photons) is not simulated. This exclusion of the electromagnetic component may result in an underestimation of the total muon flux.

The spectra obtained via the prompt tagging, described in Section 3, agree well with MCEq predictions, as shown in Figure 1. The uncertainties shown for the CORSIKA7 simulation are the standard deviation of the sum of weighted Poisson-distributed events, computed as  $\sigma = \sqrt{\sum_i w_i^2}$  [26]. The agreement indicates that the tagging procedure works as intended and that CORSIKA7 can indeed be used to identify prompt muons. A more in-depth comparison of different decay channels is studied in the following section.

### 3.2 A Muon’s Genealogy

Previously, the prompt atmospheric flux was defined by muons from charm hadron decays (mainly  $D^\pm$ ,  $D^0$ ,  $\bar{D}^0$ , and  $\Lambda_c$ ) [28–30]. In the

past decade, it has been recognized that unflavored meson decays (mainly  $\eta$ ,  $\eta'$ ,  $\rho^0$ ,  $\omega$ , and  $\phi$ ) contribute to the flux at a similar scale as charm decays [11, 31]. Charmed and conventional decays also produce neutrinos, as illustrated in their tree-level Feynman diagrams in Figure 2a. In contrast, unflavored decays do not produce neutrinos, as shown in Figure 2b. This distinction can be exploited experimentally by investigating ratios of measured muon and neutrino spectra to differentiate these contributions.

Differentiating the muon’s genealogy at ground level on a per-event basis is not feasible with CR-observatories, as the detector response for a muon is independent of its decay history. Probing muon production processes per event is only possible in collider experiments like those at CERN’s LHC [32–35]. LHC experiments can measure hadron decay rates, providing crucial input to MC event generators such as SIBYLL. EAS simulations can link these event generators to measured atmospheric lepton fluxes, enabling indirect measurements with CR-observatories. The tagging procedure discussed in Section 3 preserves the lepton’s decay history in the simulation chain, enabling decay-channel-specific analyses.

As shown in Figure 1, reconstructing the muon decay history with CORSIKA7 agrees with MCEq predictions at the level of differentiating between the prompt and conventional components. However, splitting the conventional muon flux into contributions from  $\pi^\pm$  or  $K^\pm$  decays using CORSIKA7 is not possible: Due to the aforementioned edge-cases caught with the HGC, EHISTORY only provides sufficient information to infer that a parent particle is conventional (i.e., a pion or kaon), but not which one it is. Nonetheless, further division of the prompt component into origins from multiple other particles is possible.

This can be compared to MCEq results displayed in Figure 3. The solid lines show the MCEq solutions from [20]. Notably, the two methods do not agree for every particle. The two particle types with the largest differences are  $D_s$  and  $D^0$ . The LHCb collaboration reports a production cross-section for  $D^0$  of  $(2072 \pm 2 \pm 124) \mu\text{b}$  in  $pp$  collisions at a center-of-mass energy of  $\sqrt{s} = 13 \text{ TeV}$ , corresponding to a fixed-target energy of  $E_{\text{FT}} \approx 90 \text{ PeV}$  [36]. Simultaneously, the production cross-section for  $D_s^+$  is much lower at  $(353 \pm 9 \pm 76) \mu\text{b}$ , while both have similar decay rates into muons.

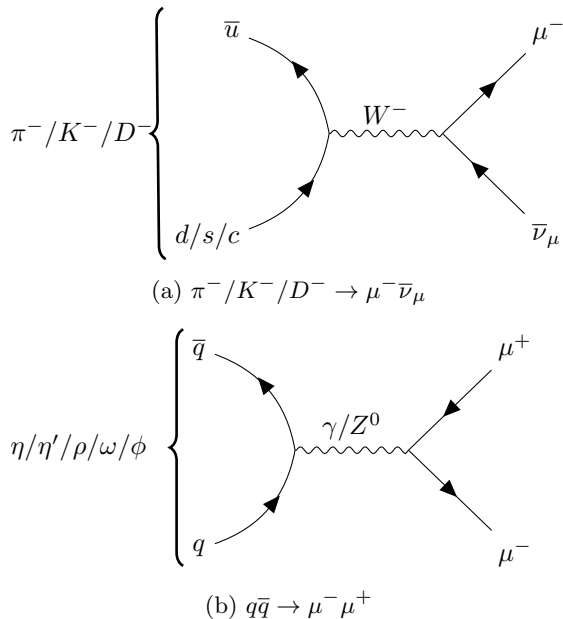


**Fig. 2:** Leading order Feynman diagrams for the  $\pi^- \rightarrow \mu^- \bar{\nu}_\mu$  decay (Figure 2a) and unflavored decays of the type  $q\bar{q} \rightarrow \mu^- \mu^+$  (Figure 2b) are displayed. The  $K^-$  ( $D^-$ ) decay has the same leading order diagram as in Figure 2a, but the down (up) quark is swapped with a strange (charm) quark.

The  $D^0$  decays into muons ( $6.8 \pm 0.6$ )% of the time, and the  $D_s^\pm$  decays into muons (assuming lepton flavor universality) ( $6.33 \pm 0.15$ )% of the time [37]. The data is provided in a pseudorapidity range of  $2 < y < 4.5$ , but extrapolation to the extreme forward boosted region of EAS should not significantly alter these ratios. The fixed-target energy lies in the relevant region for prompt muons. Therefore, these comparisons to production cross-sections, along with discussions with the authors of Ref. [20], suggest a possible error in the labeling of the MCEq results [20]. While some differences between the two methods remain, this demonstrates the advantage of having independent methods to verify each other, even if only the total flux can be experimentally observed.

### 3.3 Influence of the Primary Model

The parametrization and composition of the primary CR flux impact the prompt component of atmospheric lepton fluxes, with model differences

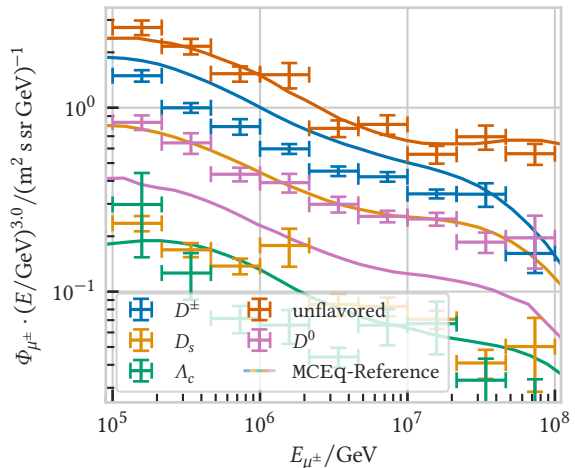


**Fig. 3:** The prompt component of the high-energy muon flux divided into different parent-particles is shown. The crosses come from the described CORSIKA7 EHIStory readout, while the solid lines come from numerical solutions to the cascade equations from MCEq. The MCEq data are taken from [20] and both simulations use the Gaisser H3a model at a zenith angle of  $60^\circ$ .

increasing with higher energies due to experimental uncertainties at very high energies. Results for the prompt muon flux from CORSIKA7 and MCEq for four different primary models are displayed in Figure 4. The Global Spline Fit (GSF) [38] and GST [39] models produce the highest prompt muon fluxes, whereas the Gaisser H3a (Population 3 is mixed) and H4a (Population 3 is proton only) models [27] yield lower prompt fluxes. Population 3 refers to the third group of CR sources, hypothesized to be supernova remnants or other astrophysical objects that predominantly contribute protons and mixed compositions at the highest energies.

Unlike the other models, the GSF model provides fluxes for every individual nucleus in the CR spectrum (although the spectral shapes are constant within groups of nuclei), while the others model the fluxes of a whole range of particles using only five nuclei. Since these five components are injected in the CORSIKA7 simulation, it calculates the same cascades as MCEq for the five-component models. For GSF, MCEq solves the equations for every single primary nucleus, whereas CORSIKA7 must marginalize the fluxes of many nuclei into groups to obtain the correct weights for the five

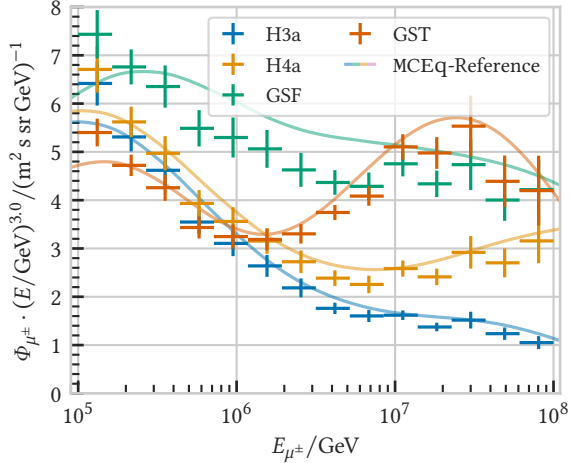


**Fig. 4:** The prompt muon flux, calculated with CORSIKA7 and EISTORY (crosses) and MCEq (lines), is compared for different primary models.

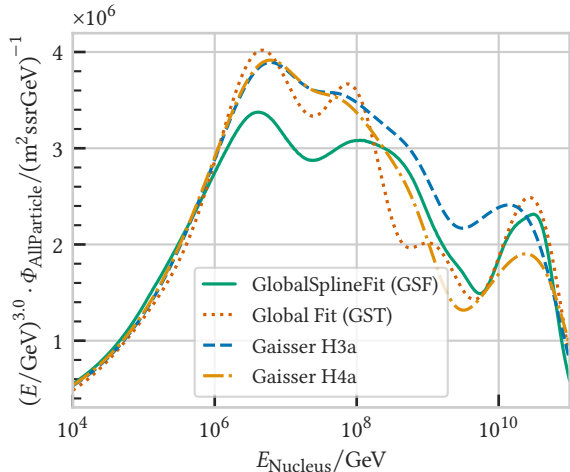


**Fig. 5:** The nucleus flux is shown for each of the utilized primary models.

components. Consequently, the primary particles used for GSF differ between MCEq and CORSIKA7, which may explain the differences between the two methods observed in Figure 4.

Figure 5 presents a comparison of the nuclei fluxes among the different primary models. The extent to which these models produce prompt muons can be understood through their varying compositions, which lead to significantly different energies per nucleon.

## 4 How to Measure the Prompt Atmospheric Lepton Fluxes

This section outlines how the described tagging method can be utilized to measure the prompt and conventional components using large-volume sub-surface detectors such as KM3NeT [7, 8] or IceCube [5, 6].

In such detectors, only muons and neutrinos can penetrate deep enough to reach the instrumented volume. A single high-energy EAS typically generates a large number of muons that arrive at the detector with lateral separations of only a few meters, or even less for higher-energy muons. These detectors generally cannot resolve individual muons in such bundles; however, often a *leading muon*, a single high-energy muon that carries most of the bundle energy, dominates the observed signal. Detector observables sensitive to the muon or neutrino flux may be utilized in an unfolding approach [40] or in a forward-folding analysis, as described in the following paragraphs. Relevant observables for differentiating the prompt and conventional components include the deposited energy, the zenith angle, and the seasonal rate [11, 20].

To measure the prompt flux contribution, the event count  $k_m$  in a particular observable bin  $m$  can be compared to the expected event count  $\lambda_m$  based on CORSIKA7 simulations. Using the tagging procedure described in Section 3, the expected event count can be decomposed into prompt ( $\lambda_m^{\text{pr}}$ ) and conventional ( $\lambda_m^{\text{conv}}$ ) contributions:

$$\lambda_m(\eta, \xi) = \lambda_m^{\text{conv}}(\eta_{\text{conv}}, \xi) + \lambda_m^{\text{pr}}(\eta_{\text{pr}}, \xi), \quad (3)$$

where  $\xi$  represents nuisance parameters such as detector systematics, and  $\eta$  includes signal parameters that influence the prompt and conventional components. These parameters can, for instance, contain the utilized hadronic interaction model and its tunable parameters, the spectral index of the component, or the overall flux normalization. For simplicity, systematic uncertainties are disregarded and it is assumed that  $\eta = \{n_{\text{conv}}, n_{\text{pr}}\}$  only consists of the overall normalization of the conventional and prompt flux components,  $n_{\text{conv}}$  and  $n_{\text{pr}}$  respectively. These are defined as scaling factors of the baseline model prediction:

$$\lambda_m^{\text{pr}}(n_{\text{pr}}) = n_{\text{pr}} \cdot \lambda_m^{\text{pr}}, \quad n_{\text{pr}} \geq 0 \quad (4)$$

where  $n_{\text{pr}} = 0$  corresponds to the absence of a prompt flux. The scaling factor  $n_{\text{conv}}$  is defined analogously.

Assuming Poisson statistics in each of the  $M$  observable bins, the likelihood of observing the data  $k_m$  is then given by

$$\mathcal{L}(n_{\text{pr}}, n_{\text{conv}}) = \prod_{m=1}^M p_{\lambda=\lambda_m}(k = k_m), \quad (5)$$

with the Poisson distribution  $p_{\lambda}(k)$ .

The scale parameters that maximize the likelihood are denoted as  $\hat{n}_{\text{conv}}$  and  $\hat{n}_{\text{pr}}$ . The null hypothesis of  $n_{\text{pr}} = 0$  may be tested via a likelihood-ratio test with the test statistic

$$\Lambda = -2 \ln \frac{\mathcal{L}(n_{\text{pr}} = \hat{n}_{\text{pr}}, n_{\text{conv}} = \hat{n}_{\text{conv}})}{\mathcal{L}(n_{\text{pr}} = 0, n_{\text{conv}} = \hat{n}_{\text{conv}})}. \quad (6)$$

The described analysis requires that the flux components may be scaled up and down according to Equation (4). There are several approaches to achieve this:

1. The parameters of the underlying hadronic interaction models may be tuned to effectively achieve scaling of the prompt flux.
2. Prompt particles passed from the underlying hadronic interaction model to CORSIKA7 may be replaced with conventional particles.
3. A complete shower is tagged as either a prompt or conventional shower and then re-weighted based on the defined scale parameters.

The first approach enables evaluation of the correlation between adjustable parameters of hadronic interaction models and the resulting lepton fluxes. However, it is the most challenging method, requiring an in-depth understanding of the model due to the non-trivial and high-dimensional dependence between the parameters and the normalization of the resulting prompt flux component.

The second solution is to replace a given prompt parent particle, e.g., a  $D^0$ , with probability  $1 - n_{\text{pr}}$  by a kaon or pion while ensuring energy and momentum conservation. Modifying the particle stack in CORSIKA7 is most effectively achieved via DYNSTACK [41]. This method, which allows setting  $n_{\text{pr}}$  between 0 and 1, is implemented here as an example and is referred to as the DYNSTACK replacement method.

The primary limitation of these two scaling approaches is the need to re-run computationally expensive CORSIKA7 simulations for each modified scale parameter value  $n_{\text{pr}}$ , rendering these methods impractical. In contrast, the third approach reuses existing simulations by re-weighting entire showers based on specified values of  $n_{\text{pr}}$  and  $n_{\text{conv}}$ . In this method, each entire EAS is classified as either a prompt or conventional shower based on the *leading muon*, defined as the most energetic muon in the shower. This is an approximate solution because all muons in a given shower, regardless of their genealogy, are re-weighted by  $n_{\text{pr}}$  or  $n_{\text{conv}}$  based on the classification of the leading muon.

Nevertheless, as shown in Figure 10, in the energy range from 100 TeV to 100 PeV, the total muon flux is dominated by leading muons between 91% to 99%. If the leading muon is prompt in this range, it dominates the flux by 92%. Figure 6 shows that the fraction of the conventional muon flux caused by conventional muons inside a prompt-tagged  $\theta = 60^\circ$  shower and vice versa is below 1.5%. The fraction of the total muon flux mistagged this way is below 1%. Falsely scaling accompanying muons in the same EAS therefore only has a minor impact on the obtained muon spectrum at these energies. This is further demonstrated in Figure 7, which compares the re-weighting approach to the DYNSTACK replacement method. The down-scaling method demonstrates that re-weighting the prompt component does not significantly impact the conventional component within statistical uncertainties. The DYNSTACK method shows a lower conventional flux above 10 PeV. This reduction may be attributed to the removal of prompt particles that would otherwise produce additional conventional particles in the atmosphere by re-interaction at extremely high energies.

## 5 Properties of the Prompt Component

The tagging method introduced in Section 3 enables differentiation of the muon flux in its individual components, as demonstrated in Section 3.1. Furthermore, a full MC simulation in CORSIKA7 enables further insights to the relevance

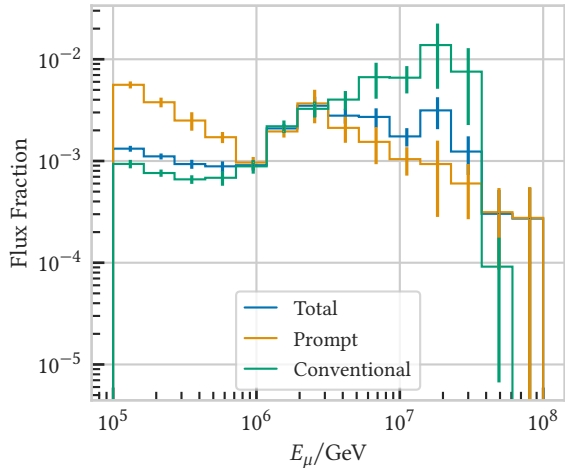


**Fig. 6:** The fraction of the muon flux which is misattributed if the prompt/conventional tag for every muon in the shower is based on the most energetic (leading) muon. The  $60^\circ$  dataset is weighted with the Gaisser H3a model. For example, the orange line shows the fraction of the prompt flux contained in showers where the leading muon is a conventional particle.

of the leading muon in a shower, the contribution of prompt and conventional muons inside a single shower, shower variations and the lateral distribution.

## 5.1 Relation to the Primary Energy

Prompt muons tend to reach higher energies, dominating the total muon flux above approximately 1 PeV. While this might suggest that prompt muons carry a greater fraction of energy from the primary particle than their conventional counterparts, the opposite is true. This is demonstrated in Figure 8, where the average fraction of the primary energy a muon carries is shown in each muon energy bin for both prompt and conventional particles. The lower panel displays the ratio between the prompt and conventional averages. While there are large shower-to-shower fluctuations, this shows that on average prompt muons carry a smaller fraction of their primaries' energy than conventional muons. The last bin has a ratio of 90% between the two components, which could in part be due to the smaller statistics of conventional muons at these energies. In the other bins, the prompt muons carry approximately only

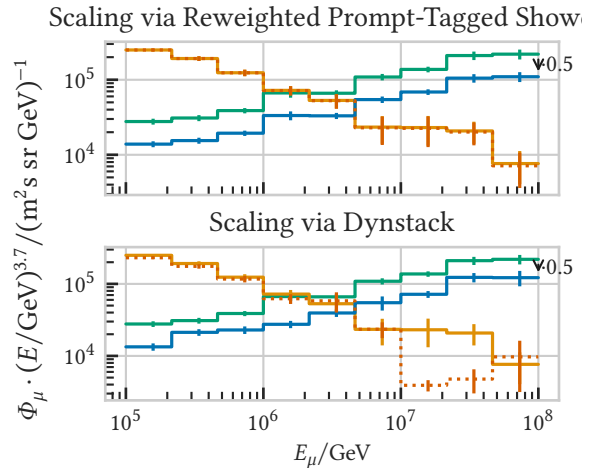


**Fig. 7:** Two methods for scaling the prompt component of the muon flux at  $\theta = 60^\circ$  are compared. The green histogram represents the baseline prompt component produced by standard CORSIKA7 simulations, while the blue histogram shows the prompt component downscaled by a factor of 0.5. The orange histogram depicts the conventional component, and the orange dotted histogram illustrates how scaling the prompt component affects the conventional one. The upper panel demonstrates scaling by applying an additional weight of 0.5 to events (showers) tagged as prompt, whereas the lower panel shows the scaling method implemented via DYNSTACK, where a new simulation dataset is generated by explicitly replacing prompt particles with conventional ones during the simulation. The H3a CR model is used for weighting.

between 35% to 70% as much of the primaries' energy as conventional ones.

## 5.2 Relation to the Primary Flux

Theoretical calculations of lepton fluxes at sea level using the  $Z$ -moment method provides results for lepton fluxes from each parent particle type  $H$  in the form of [29]

$$\Phi_\mu(E_\mu, \theta) = \Phi_p(E_\mu) \frac{\mathcal{A}}{1 + \mathcal{B} \frac{E_\mu}{\epsilon_h} \cos \theta}, \quad (7)$$

where  $\Phi_p$  is the primary flux at the muon energy and  $\epsilon_h$  is the critical energy for a given parent hadron. For prompt particles, the relation

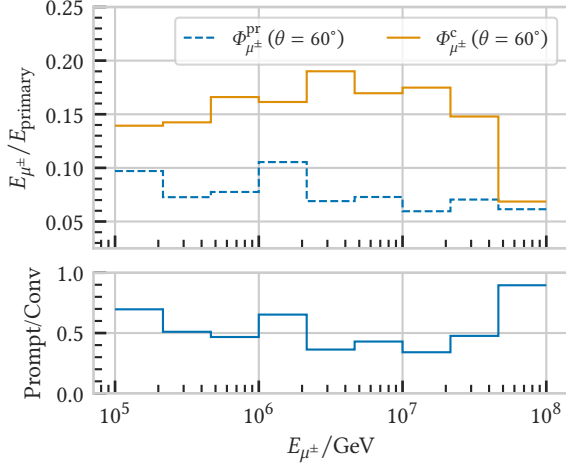


**Fig. 8:** The energy bin-wise average of the ratio of the muon energy to the primary energy. The events are weighted according to the H3a primary model. The lower panel shows the ratio of the prompt average to the conventional mean value.

$E_\mu \ll \epsilon_h$  holds and Equation (7) simplifies to the known relation  $\Phi_\mu \propto \Phi_p$ . For conventional particles,  $E_\mu \gg \epsilon_h$  is valid, leading to the relation  $\Phi_\mu \propto \Phi_p / (E_\mu \cos \theta)$ . The factors  $\mathcal{A}$  and  $\mathcal{B}$  contain the spectrum weighted  $Z$ -moments and they are also energy dependent, although this energy-dependency is not very large compared to  $1/E_\mu$ . This behavior is approximately asserted in Figure 9, where indeed the  $1/E_\mu$  slope of the conventional component is visible.

To assert that the values shown in Figure 9 are consistent with theoretical predictions, the values given in Ref. [42] are translated to the values shown in that figure. Equation (7) in the region below the critical energy is approximated by

$$\frac{\Phi_\mu}{\Phi_p} \approx \mathcal{A} = Z_{H\mu} \frac{Z_{NH}^d}{1 - Z_{NN}}.$$

Estimating from Figure 9 from Ref. [42], the  $Z_{NH}$  ranges between approximately  $1.3 \cdot 10^{-4}$  to  $3.5 \cdot 10^{-4}$  for the sum of charmed hadrons  $D^0, D^+, D_s^+, \Lambda_c^+$ . Energy-dependent  $Z_{NN}$  values from Ref. [43] provide  $Z_{NN} = 0.271$  at  $E = 10^3$  GeV and  $Z_{NN} = 0.231$  at  $E = 10^8$  GeV. As neither Ref. [42] nor Ref. [43] provide their calculated values for  $Z_{H\mu}$  directly,  $Z_{D\mu} \approx 0.03$  is estimated based on Appendix A from Ref. [30], which both papers provide as a reference. This

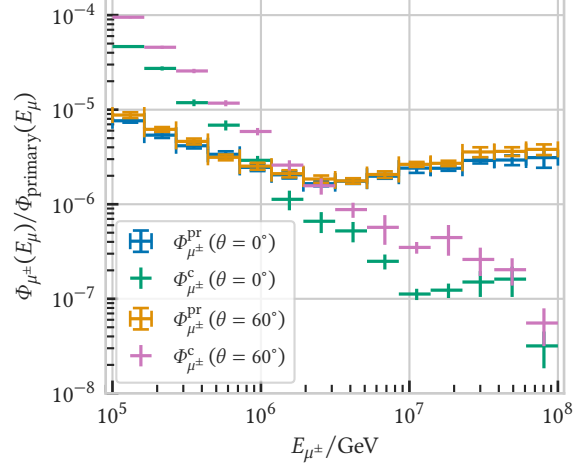


**Fig. 9:** The muon flux (weighted using H3a), divided by the primary particle flux *at the muon's energy*, is binned. The spectrum is separated into the prompt (pr) and conventional (c) components for  $0^\circ$  and  $60^\circ$ . The prompt component shows an approximately flat shape up to  $10^8$  GeV, while the conventional component exhibits an approximate proportionality to  $E^{-1}$ .

results in an estimate at the lower energy range of

$$\mathcal{A} = 5.7 \cdot 10^{-6}$$

and at the higher end of the energy range of

$$\mathcal{A} = 1.4 \cdot 10^{-5}.$$

These values are approximately consistent with the flux fraction of the prompt component seen in Figure 9, which is on the order of  $10^{-5}$ .

### 5.3 Leadingness of Prompt Muons

Since detectors measure only the combined muon flux of a muon bundle, the significance of the leading muon within the bundle is examined in Figure 10. For the energy range from  $10^5$  GeV to  $10^8$  GeV, the contribution of the leading muon to the entire muon flux per energy bin is above 91%. If the leading muon is conventional in this energy range, the flux is dominated by more than 99%. If the leading muon is prompt, the flux is dominated by more than 90%. Since the prompt component becomes more relevant towards higher energies, in

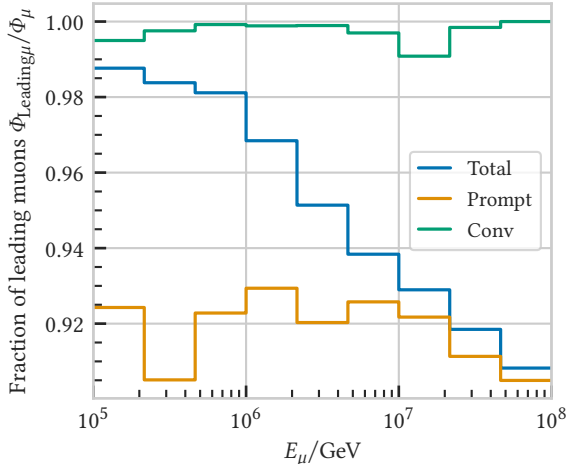


**Fig. 10:** The leading muon flux divided by the total muon flux per energy bin is shown by the blue line. Also the fraction of leading muons per energy bin, separated into prompt and conventional components, is shown. For example, a value of 0.9 in a given bin indicates that 90% of the total muon flux in this energy bin originates from leading muons. If the leading muon is conventional for the shown energy range, the entire flux is dominated by more than 99%. A leading muon is defined as the most energetic muon within a shower. H3a-weighting is used.

this energy range, the blue total curve converges to the orange prompt line.

## 5.4 Lateral Distribution

Another way to study the prompt component is to examine the lateral distribution. Since prompt parent particles are at least an order of magnitude heavier than pions ( $m_{D^+}/m_{\pi^+} \approx 13$ ), their Lorentz factor is smaller at the same energy, allowing prompt particles to reach greater lateral distances from the shower axis due to reduced forward boosting. With the full MC simulation presented here, the lateral distribution of prompt versus conventional muons can be analyzed. Figure 11 illustrates the lateral distribution of prompt and conventional muons above 1 PeV for down-going EAS. This 1 PeV threshold is selected to yield comparable statistics for both particle types. However, at these energies, the distributions are on

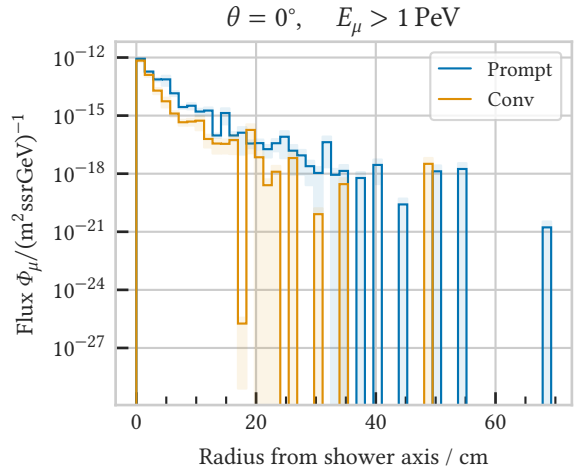


**Fig. 11:** The lateral flux-distribution of conventional and prompt muons above 1 PeV for down going showers. The H3a CR flux model is used. Prompt muons are expected to have wider distribution since their parents are less forward boosted compared to their conventional counterparts.

the order of centimeters, making it experimentally challenging to distinguish between prompt and conventional muons based on lateral spread.

## 6 Conclusions

This work presents and validates a tagging procedure for distinguishing atmospheric leptons originating from the decay of different types of particles in CORSIKA7 simulations. The conventional lepton flux arises from pion and kaon decays, while the prompt flux arises from all other decays. The method leverages CORSIKA7's extended history option in conjunction with the newly developed PANAMA software package. Tagged conventional and prompt muon flux components demonstrate good agreement with MCEq, as presented in Figure 1, Figure 3 and Figure 4. This tagging method allows not only for an independent verification method to existing tools such as MCEq, but also enables the study of properties unavailable to solutions of the analytical cascade equations, such as shower-to-shower fluctuations, the lateral distribution of final-state leptons and their leadingness.

For the energy range from  $10^5$  GeV to  $10^8$  GeV, on average, prompt muons carry between 35% and 90% as much of the primary energy as

conventional muons, as presented in Figure 8. Theoretical calculations using the  $Z$ -moment method confirm that prompt muons closely follow the primary flux, while conventional muons decrease with energy as  $1/E_\mu$ , aligning well with observed muon flux distributions. The estimated fractions of the muon fluxes divided by the primary flux are consistent with the prompt flux component shown in Figure 9, at approximately  $10^{-5}$ . Additionally, analysis of the leading muon’s contribution shows it accounts for over 91% of the total muon flux across energy bins (Figure 10). A study of the lateral distribution indicates that the spatial spread difference between prompt and conventional muons is minimal, on the order of centimeters, making experimental resolution challenging (Figure 11).

Appendix B provides parametrizations for the conventional, charm, unflavored and other prompt muon flux as a function of the muon energy at the surface for different primary weightings.

Additionally, we propose an analysis method in Section 4 to obtain the normalization of the prompt muon flux, which could constrain parameters of hadronic interaction models within a phase space of energies and pseudorapidities beyond the reach of current accelerators. Future studies based on this approach may thus play an essential role in resolving the muon puzzle and advancing our understanding of CR interactions.

**Acknowledgments.** We acknowledge support from the Deutsche Forschungsgemeinschaft (DFG, German Research Foundation), via the Collaborative Research Center SFB1491 ”Cosmic Interacting Matters - From Source to Signal” (project No. 445052434) and the Bundesministerium für Bildung und Forschung (BMBF, Federal Ministry of Education and Research). We also thank Hans Dembinski for fruitful discussions, and Agnieszka Leszczyńska and Jonathan Meßner for helpful insights on the HGC, as well as Anatoli Fedynitch and Tanguy Pierog for valuable feedback on MCEq and CORSIKA7.

## Appendix A Simulated Dataset

Listing 1: CORSIKA7 steering card for the test dataset used in this work. The templates marked with  $\{\dots\}$  are replaced accordingly.

```

RUNNR    {run_idx}
EVTNR    {first_event_idx}
NSHOW    {n_show}
PRMPAR   {primary}
ESLOPE   -1
ERANGE   {emin} {emax}
THETAP   0.    0.
PHIP     -180. 180.
SEED     {seed_1} 0    0
SEED     {seed_2} 0    0
OBSLEV   110.E2
FIXCHI   0.
MAGNET   16.811 -51.890
HADFLG   0 0 0 0 0 2
ECUTS    1.E5 1.E5 1.E20 1.E20
MUADDI   T
MUMULT   T
ELMFLG   T    T
STEPFC   1.0
RADNKG   200.E2
LONGI    F 10.  F  F
MAXPRT   1
DIRECT   {dir}
DYNSTACK 10000
DYNSTACK_P 1 1
USER     you
DEBUG    F 6  F  1000000
EXIT

```

## Appendix B Fitting the Muon Flux

Parameterizing the high-energy muon flux from the MC simulation is useful to obtain simple analytical models for later use in generating muon MC and also for the comparison to theoretical models. The tagging procedure described earlier allows to parameterize different components of the muon flux independently. The muon spectrum is divided into four components: The conventional, the charmed, the unflavored and other parts of the prompt spectrum, including muons directly created at an interaction vertex. To find

an appropriate model, the low energy

$$\Phi_{H \rightarrow \mu}^{\text{low}E} = Z_{H\mu}^d \frac{Z_{pH}}{1 - Z_{pp}} \cdot \Phi_N \quad (\text{B1})$$

and high energy

$$\Phi_{H \rightarrow \mu}^{\text{high}E} = Z_{H\mu}^d \frac{Z_{pH}}{1 - Z_{pp}} \frac{\ln(\Lambda_H/\Lambda_p)}{1 - \frac{\Lambda_p}{\Lambda_H}} \frac{\epsilon_H}{E_H} f(\theta) \cdot \Phi_N \quad (\text{B2})$$

solutions of the cascade equations, as well as their usual interpolation

$$\Phi_{\mu}^{\text{tot}} = \Phi_N \sum_H \frac{\mathcal{A}_{HL}}{1 + \mathcal{B}_{HL} \frac{E}{\epsilon_H f(\theta)}} \quad (\text{B3})$$

are considered [11, 44]. Since these solutions are proportional to the initial nucleon flux  $\Phi_N$ , the flux is parameterized in terms of the fraction of the primary flux model  $\Phi_{\mu}/\Phi_N$ . The zenith-dependency  $f(\theta)$  is assumed to be accurately modeled by  $f(\theta) = 1/\cos(\theta^*(\theta, h = 50\text{km}))$ , and only the  $\theta = 0^\circ$  dataset is used for the fit, which reduces the number of fitted dimensions to one.

Since the simulation is optimized for prompt contributions, ranging below the prompt cross over at  $E = 10^5\text{GeV}$  to  $E = 10^8\text{GeV}$ , simplifications to the model are introduced. For the conventional part, only the high-energy solution is relevant, since  $E \gg \epsilon_{\text{conv}}$ , so that the used model becomes

$$m_{\text{conv}}(E) = \Phi_{\text{conv} \rightarrow \mu} / \Phi_N = \frac{\epsilon_{\pi^\pm}}{E} f(\theta) P(\log E) \quad (\text{B4})$$

where  $P(\log E)$  is a function describing the energy dependency of the  $Z$  and  $\Lambda$  factors in Equation (B2), which are seen to vary logarithmically with energy in Ref. [44]. For the unflavored and other prompt particles the opposite is the case, and the high energy limit can be neglected, since  $E \ll \epsilon_{\text{unfl.}}$ , arriving at a model

$$m_{\text{unfl./other}} = \Phi_{\text{unfl./other} \rightarrow \mu} / \Phi_N = P(\log E). \quad (\text{B5})$$

Only for the charm component the transition energy  $\epsilon_{D^\pm} \approx 30\text{PeV}$  is in the energy range of the simulation. Here the form of Equation (B3)

$$m_{\text{charm}} = \Phi_{\text{charm} \rightarrow \mu} / \Phi_N = \frac{P(\log E)}{1 + B \frac{E}{\epsilon_{D^\pm} f(\theta)}} \quad (\text{B6})$$

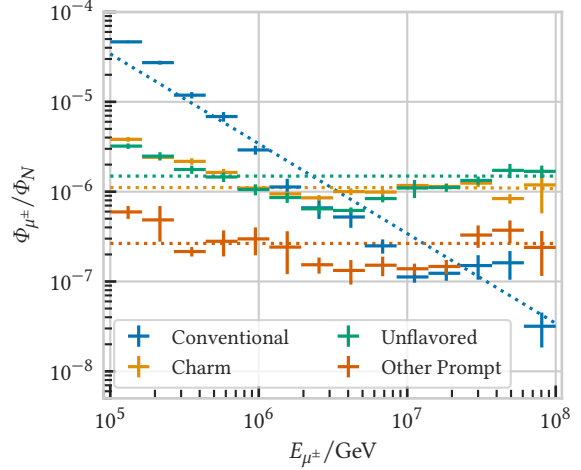


**Fig. B1:** Simple weighted, binned, extended likelihood fit assuming Feynman scaling. The CR flux model is H3a.

is used. The possible energy-dependency of  $B$  is neglected, since the statistics in the PeV region is so small that resolving any dependency is not possible.

The fits are performed as a weighted, binned, extended likelihood fit, since the flux can be understood as the relative probability of finding a particle at the given energy. This is performed using the python package `iminuit` [45], which provides modern python bindings to the `iminuit 2`, `hesse` and `migrad` fitting routines of CERN's `root` library. Error estimation is performed using the `hesse` algorithm. The probability distribution of weighted poissonian bin counts is given by Bohm and Zech in Ref. [26], where the suggested approximate transformation (Bohm-Zech transformation) to a poisson random variable is performed by `iminuit`.

If Feynman scaling is assumed in the calculation of the  $Z$  and  $\Lambda$  factors, all energy dependency is lost and the correction functions become constant  $P(\log E) = A$ . The fits using this approximation are visualized in Figure B1, and the parameters are listed in Table B1.

To include the energy dependency of the spectrum weighted moments  $Z$  and  $\Lambda$ , a form for their dependency has to be assumed. No analytical form of this dependency exists, but in Ref. [42] the different  $Z_{\text{charm}}$  have one local maximum and one local minimum in the used energy range, which

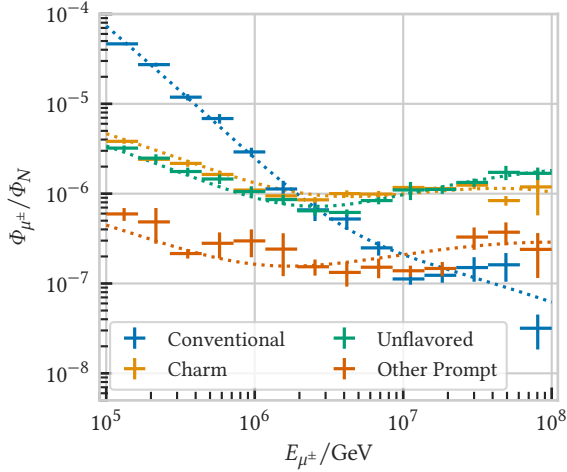


**Fig. B2:** Weighted, binned, extended likelihood fit assuming an energy dependency in the form of a third order polynomial. The CR flux model is H3a.

makes the assumption of a third order polynomial  $P(\log E) = a \log^3 E + b \log^2 E + c \log E + A$  a reasonable choice. The fits with this assumption are shown in Figure B2. The minimization algorithm is initialized with values from a previous  $\chi^2$ -fit, to help migrad find the minimum faster. The fit-values are found in Table B2.

**Table B1:** Obtained parameters for the fit of the muon spectrum in different components using the model which assumes Feynman scaling, as described in Section B.

	Conventional	Charm	Unflavored	Other Prompt
H3a				
$A$	3.42	$1.11 \cdot 10^{-6}$	$1.49 \cdot 10^{-6}$	$2.65 \cdot 10^{-7}$
$B$	-	$2.64 \cdot 10^{-2}$	-	-
$\chi^2/n_{\text{DOF}}$	38.74	27.16	49.13	8.66
H4a				
$A$	4.36	$2.22 \cdot 10^{-6}$	$2.39 \cdot 10^{-6}$	$3.74 \cdot 10^{-7}$
$B$	-	$2.37 \cdot 10^{-3}$	-	-
$\chi^2/n_{\text{DOF}}$	32.69	60.30	98.91	13.48
GSF				
$A$	4.88	$2.14 \cdot 10^{-6}$	$1.99 \cdot 10^{-6}$	$3.87 \cdot 10^{-7}$
$B$	-	$4.76 \cdot 10^{-1}$	-	-
$\chi^2/n_{\text{DOF}}$	23.64	19.89	21.93	6.40
GST				
$A$	6.44	$5.50 \cdot 10^{-6}$	$3.34 \cdot 10^{-6}$	$6.67 \cdot 10^{-7}$
$B$	-	1.91	-	-
$\chi^2/n_{\text{DOF}}$	33.65	596.26	153.49	31.87

**Table B2:** Obtained parameters for the fit of the muon spectrum in different components. The fitted model parameterizes the energy-dependency of the  $Z$ -factor, as described in Section B.

	Conventional	Charm	Unflavored	Other Prompt
H3a				
$A$	$9.91 \cdot 10^1$	$1.59 \cdot 10^{-4}$	$1.18 \cdot 10^{-4}$	$1.71 \cdot 10^{-5}$
$B$	-	$1.05 \cdot 10^{-6}$	-	-
$a$	$2.79 \cdot 10^{-6}$	$-3.60 \cdot 10^{-8}$	$-2.46 \cdot 10^{-8}$	$-4.02 \cdot 10^{-9}$
$b$	$4.23 \cdot 10^{-1}$	$1.77 \cdot 10^{-6}$	$1.26 \cdot 10^{-6}$	$1.98 \cdot 10^{-7}$
$c$	$-1.28 \cdot 10^1$	$-2.90 \cdot 10^{-5}$	$-2.12 \cdot 10^{-5}$	$-3.19 \cdot 10^{-6}$
$\chi^2/n_{\text{DOF}}$	5.96	7.22	1.73	3.95
H4a				
$A$	$9.96 \cdot 10^1$	$3.08 \cdot 10^{-4}$	$9.01 \cdot 10^{-5}$	$1.62 \cdot 10^{-5}$
$B$	-	$2.06 \cdot 10^{-6}$	-	-
$a$	$1.00 \cdot 10^{-2}$	$-6.51 \cdot 10^{-8}$	$-1.19 \cdot 10^{-8}$	$-3.72 \cdot 10^{-9}$
$b$	$1.54 \cdot 10^{-1}$	$3.31 \cdot 10^{-6}$	$7.59 \cdot 10^{-7}$	$1.86 \cdot 10^{-7}$
$c$	$-1.11 \cdot 10^1$	$-5.54 \cdot 10^{-5}$	$-1.47 \cdot 10^{-5}$	$-3.02 \cdot 10^{-6}$
$\chi^2/n_{\text{DOF}}$	12.34	99.66	0.56	3.24
GSF				
$A$	$9.95 \cdot 10^1$	$6.36 \cdot 10^{-8}$	$1.78 \cdot 10^{-4}$	$1.94 \cdot 10^{-5}$
$B$	-	7.17	-	-
$a$	$6.35 \cdot 10^{-3}$	$3.18 \cdot 10^{-8}$	$-4.37 \cdot 10^{-8}$	$-5.52 \cdot 10^{-9}$
$b$	$2.43 \cdot 10^{-1}$	$-9.28 \cdot 10^{-7}$	$2.11 \cdot 10^{-6}$	$2.55 \cdot 10^{-7}$
$c$	$-1.15 \cdot 10^1$	$6.92 \cdot 10^{-6}$	$-3.36 \cdot 10^{-5}$	$-3.86 \cdot 10^{-6}$
$\chi^2/n_{\text{DOF}}$	9.58	2.81	3.75	5.30
GST				
$A$	$1.00 \cdot 10^2$	$4.89 \cdot 10^{-4}$	$4.90 \cdot 10^{-4}$	$3.47 \cdot 10^{-4}$
$B$	-	3.48	-	-
$a$	$1.00 \cdot 10^{-2}$	$-1.47 \cdot 10^{-7}$	$-1.49 \cdot 10^{-7}$	$-9.06 \cdot 10^{-8}$
$b$	$2.05 \cdot 10^{-1}$	$6.72 \cdot 10^{-6}$	$6.73 \cdot 10^{-6}$	$4.28 \cdot 10^{-6}$
$c$	$-1.17 \cdot 10^1$	$-1.00 \cdot 10^{-4}$	$-9.99 \cdot 10^{-5}$	$-6.69 \cdot 10^{-5}$
$\chi^2/n_{\text{DOF}}$	17.65	117.18	64.58	236.95

## References

- [1] Albrecht, J., Cazon, L., Dembinski, H., Fedynitch, A., Kampert, K.-H., Pierog, T., Rhode, W., Soldin, D., Spaan, B., Ulrich, R., *et al.*: The muon puzzle in cosmic-ray induced air showers and its connection to the large hadron collider. *Astrophysics and Space Science* **367**(3), 27 (2022) <https://doi.org/10.1007/s10509-022-04054-5>
- [2] Telescope Array Collaboration: An extremely energetic cosmic ray observed by a surface detector array. *Science* **382**(6673), 903–907 (2023) <https://doi.org/10.1126/science.abo5095>
- [3] Aab, A., *et al.*: The Pierre Auger Cosmic Ray Observatory. *Nucl. Instrum. Meth. A* **798**, 172–213 (2015) <https://doi.org/10.1016/j.nima.2015.06.058> arXiv:1502.01323 [astro-ph.IM]
- [4] Aab, A., *et al.*: Testing Hadronic Interactions at Ultrahigh Energies with Air Showers Measured by the Pierre Auger Observatory. *Phys. Rev. Lett.* **117**(19), 192001 (2016) <https://doi.org/10.1103/PhysRevLett.117.192001>
- [5] IceCube Collaboration: The IceCube Neutrino Observatory: instrumentation and online systems. *Journal of Instrumentation* **12**(03), 03012–03012 (2017) <https://doi.org/10.1088/1748-0221/12/03/p03012>
- [6] Verpoest, S., *et al.*: Testing Hadronic Interaction Models with Cosmic Ray Measurements at the IceCube Neutrino Observatory. *PoS ICRC2021*, 357 (2021) <https://doi.org/10.22323/1.395.0357> arXiv:2107.09387 [astro-ph.HE]
- [7] KM3NeT Collaboration: Letter of intent for km3net 2.0. *Journal of Physics G: Nuclear and Particle Physics* **43**(8), 084001 (2016) <https://doi.org/10.1088/0954-3899/43/8/084001>
- [8] KM3NeT Collaboration: Atmospheric muons measured with the KM3NeT detectors in comparison with updated numeric predictions. *European Physical Journal C* **84**, 696 (2024) <https://doi.org/10.1140/epjc/s10052-024-13018-8>
- [9] Heck, D., Knapp, J., Capdevielle, J.N., Schatz, G., Thouw, T.: Corsika: A monte carlo code to simulate extensive air showers. Technical report (1998). <https://doi.org/10.5445/IR/270043064> . 51.02.03; LK 01; Wissenschaftliche Berichte, FZKA-6019 (Februar 98)
- [10] Fedynitch, A., Engel, R., Gaisser, T.K., Riehn, F., Stanev, T.: Calculation of conventional and prompt lepton fluxes at very high energy (2015). <https://doi.org/10.1051/epjconf/20159908001>
- [11] Gaisser, T.K., Engel, R., Resconi, E.: *Cosmic Rays and Particle Physics*, 2nd edn. Cambridge University Press, Cambridge (2016). <https://doi.org/10.1017/CBO9781139192194>
- [12] Aaij, R., Beteta, C.A., Ackernley, T., Adeva, B., Adinolfi, M., Afsharnia, H., Aidala, C.A., Aiola, S., Ajaltouni, Z., *et al.*: Measurement of prompt charged-particle production in pp collisions at a centre-of-mass energy of 13 tev. *Journal of High Energy Physics* **2022**(1) (2022) [https://doi.org/10.1007/jhep01\(2022\)166](https://doi.org/10.1007/jhep01(2022)166)
- [13] U.S. Department of Energy: Doe fundamentals handbook. Technical report (January 1993). [https://www.navsea.navy.mil/Portals/103/Documents/NNPTC/Physics/doe\\_phys\\_nuc.pdf](https://www.navsea.navy.mil/Portals/103/Documents/NNPTC/Physics/doe_phys_nuc.pdf)
- [14] Aartsen, M.G., *et al.*: Characterization of the Atmospheric Muon Flux in IceCube. *Astropart. Phys.* **78**, 1–27 (2016) <https://doi.org/10.1016/j.astropartphys.2016.01.006>
- [15] Knapp, J., Heck, D.: Extensive air shower simulation with corsika: A user’s manual. Technical report, Karlsruhe (1993). [https://www.iap.kit.edu/corsika/downloads/CORSIKA\\_GUIDE7.7550.pdf](https://www.iap.kit.edu/corsika/downloads/CORSIKA_GUIDE7.7550.pdf) Accessed 2020-07-22
- [16] Heck, D., Engel, R.: The ehistory and

- muprod options of the air shower simulation program corsika. Technical report, Karlsruher Institut für Technologie (KIT) (2013). <https://publikationen.bibliothek.kit.edu/1000034601>
- [17] Neste, L.: Panama (2023) <https://doi.org/10.5281/zenodo.10210623>
- [18] Kozynets, T., Fedynitch, A., Koskinen, D.J.: Angular distributions of atmospheric leptons via two-dimensional matrix cascade equations. *PoS ICRC2023*, 516 (2023) <https://doi.org/10.22323/1.444.0516>
- [19] Kozynets, T., Fedynitch, A., Koskinen, D.J.: Atmospheric lepton fluxes via two-dimensional matrix cascade equations. *Physical Review D* **108**(10) (2023) <https://doi.org/10.1103/physrevd.108.103040>
- [20] Fedynitch, A., Riehn, F., Engel, R., Gaisser, T.K., Stanev, T.: Hadronic interaction model Sibyll-2.3c and inclusive lepton fluxes. *Physical Review D* **100**(10) (2019) <https://doi.org/10.1103/physrevd.100.103018>
- [21] Ostapchenko, S.: Monte Carlo treatment of hadronic interactions in enhanced Pomeron scheme: I. QGSJET-II model. *Phys. Rev. D* **83**, 014018 (2011) <https://doi.org/10.1103/PhysRevD.83.014018>
- [22] Bird, D.J., Corbató, S.C., Dai, H.Y., Dawson, B.R., Elbert, J.W., Gaisser, T.K., Green, K.D., Huang, M.A., Kieda, D.B., Ko, S., Larsen, C.G., Loh, E.C., Luo, M., Salamon, M.H., Smith, D., Sokolsky, P., Sommers, P., Stanev, T., Tang, J.K.K., Thomas, S.B., Tilav, S.: Evidence for correlated changes in the spectrum and composition of cosmic rays at extremely high energies. *Phys. Rev. Lett.* **71**, 3401–3404 (1993) <https://doi.org/10.1103/PhysRevLett.71.3401>
- [23] Kampert, K.-H., Unger, M.: Measurements of the cosmic ray composition with air shower experiments. *Astroparticle Physics* **35**(10), 660–678 (2012) <https://doi.org/10.1016/j.astropartphys.2012.02.004>
- [24] Riehn, F., Engel, R., Fedynitch, A., Gaisser, T.K., Stanev, T.: Hadronic interaction model sibyll 2.3d and extensive air showers. *Physical Review D* **102**(6) (2020) <https://doi.org/10.1103/physrevd.102.063002>
- [25] Bleicher, M., *et al.*: Relativistic hadron hadron collisions in the ultrarelativistic quantum molecular dynamics model. *J. Phys. G* **25**, 1859–1896 (1999) <https://doi.org/10.1088/0954-3899/25/9/308>
- [26] Bohm, G., Zech, G.: Statistics of weighted poisson events and its applications. *Nuclear Instruments and Methods in Physics Research Section A: Accelerators, Spectrometers, Detectors and Associated Equipment* **748**, 1–6 (2014) <https://doi.org/10.1016/j.nima.2014.02.021>
- [27] Gaisser, T.K.: Spectrum of cosmic-ray nucleons, kaon production, and the atmospheric muon charge ratio. *Astroparticle Physics* **35**(12), 801–806 (2012) <https://doi.org/10.1016/j.astropartphys.2012.02.010>
- [28] Bugaev, E.V., Naumov, V.A., Sinigovsky, S.I., Zaslavskaya, E.S.: Prompt Leptons in Cosmic Rays. *Nuovo Cim. C* **12**, 41–73 (1989) <https://doi.org/10.1007/BF02509070>
- [29] Thunman, M., Ingelman, G., Gondolo, P.: Charm production and high-energy atmospheric muon and neutrino fluxes. *Astropart. Phys.* **5**, 309–332 (1996) [https://doi.org/10.1016/0927-6505\(96\)00033-3](https://doi.org/10.1016/0927-6505(96)00033-3)
- [30] Bugaev, E.V., Misaki, A., Naumov, V.A., Sinigovskaya, T.S., Sinigovsky, S.I., Takahashi, N.: Atmospheric muon flux at sea level, underground and underwater. *Phys. Rev. D* **58**, 054001 (1998) <https://doi.org/10.1103/PhysRevD.58.054001>
- [31] Illana, J.I., Lipari, P., Masip, M., Meloni, D.: Atmospheric lepton fluxes at very high energy. *Astropart. Phys.* **34**, 663–673 (2011) <https://doi.org/10.1016/j.astropartphys.2011.01.001>
- [32] Alves, A.A. Jr., *et al.*: The LHCb Detector at the LHC. *JINST* **3**, 08005 (2008) <https://doi.org/10.1088/1748-0221/3/08/S08005>

- [33] Aad, G., *et al.*: The ATLAS Experiment at the CERN Large Hadron Collider. *JINST* **3**, 08003 (2008) <https://doi.org/10.1088/1748-0221/3/08/S08003>
- [34] Chatrchyan, S., *et al.*: The CMS Experiment at the CERN LHC. *JINST* **3**, 08004 (2008) <https://doi.org/10.1088/1748-0221/3/08/S08004>
- [35] Aamodt, K., *et al.*: The ALICE experiment at the CERN LHC. *JINST* **3**, 08002 (2008) <https://doi.org/10.1088/1748-0221/3/08/S08002>
- [36] Aaij, R., *et al.*: Measurements of prompt charm production cross-sections in  $pp$  collisions at  $\sqrt{s} = 13$  TeV. *JHEP* **03**, 159 (2016) [https://doi.org/10.1007/JHEP03\(2016\)159](https://doi.org/10.1007/JHEP03(2016)159) . [Erratum: *JHEP* 09, 013 (2016), Erratum: *JHEP* 05, 074 (2017)]
- [37] Workman, R.L., Others: Review of Particle Physics. *PTEP* **2022**, 083–01 (2022) <https://doi.org/10.1093/ptep/ptac097>
- [38] Dembinski, H.P., Engel, R., Fedynitch, A., Gaisser, T., Riehn, F., Stanev, T.: Data-driven model of the cosmic-ray flux and mass composition from 10 GeV to  $10^{11}$  GeV (2018). <https://doi.org/10.22323/1.301.0533>
- [39] Gaisser, T., Stanev, T., Tilav, S.: Cosmic Ray Energy Spectrum from Measurements of Air Showers (2013). <https://doi.org/10.1007/s11467-013-0319-7>
- [40] IceCube Collaboration: Development of a general analysis and unfolding scheme and its application to measure the energy spectrum of atmospheric neutrinos with icecube. *European Physical Journal C* **75**(116) (2015) <https://doi.org/10.1140/epjc/s10052-015-3330-z>
- [41] Baack, D.: Data reduction for CORSIKA. Technical Report 2, E5b, Faculty Physics, TU Dortmund (June 2016). <https://github.com/tudo-astroparticlephysics/Cor-PlusPlus>
- [42] Garzelli, M.V., Moch, S., Sigl, G.: Lepton fluxes from atmospheric charm revisited. *Journal of High Energy Physics* **2015**(10) (2015) [https://doi.org/10.1007/jhep10\(2015\)115](https://doi.org/10.1007/jhep10(2015)115)
- [43] Bhattacharya, A., Enberg, R., Reno, M.H., Sarcevic, I., Stasto, A.: Perturbative charm production and the prompt atmospheric neutrino flux in light of RHIC and LHC. *Journal of High Energy Physics* **2015**(6) (2015) [https://doi.org/10.1007/jhep06\(2015\)110](https://doi.org/10.1007/jhep06(2015)110)
- [44] Garzelli, M.V., Moch, S., Sigl, G.: Lepton fluxes from atmospheric charm revisited. *Journal of High Energy Physics* **2015**(10), 1–37 (2015) [https://doi.org/10.1007/JHEP10\(2015\)115](https://doi.org/10.1007/JHEP10(2015)115)
- [45] Dembinski, H., Ongmongkolkul, P.: scikit-hep/iminuit (2020) <https://doi.org/10.5281/zenodo.3949207>